



Published in final edited form as:

Science. 2018 June 29; 360(6396): 1447–1451. doi:10.1126/science.aas9160.

A method for single neuron chronic recording from the retina in awake mice

Guosong Hong^{1,†}, Tian-Ming Fu^{1,†}, Mu Qiao^{2,†}, Robert D. Viveros³, Xiao Yang¹, Tao Zhou¹, Jung Min Lee^{1,4}, Hong-Gyu Park^{1,4}, Joshua R. Sanes², and Charles M. Lieber^{1,3,*}

¹Department of Chemistry and Chemical Biology, Harvard University, Cambridge, Massachusetts, USA

²Center for Brain Science and Department of Molecular and Cellular Biology, Harvard University, Cambridge, Massachusetts, USA

³John A. Paulson School of Engineering and Applied Sciences, Harvard University, Cambridge, Massachusetts, USA

⁴Department of Physics, Korea University, Seoul, Republic of Korea

Abstract

The retina, which processes visual information and sends it to the brain, is an excellent model for studying neural circuitry. It has been probed extensively *ex vivo*, but has been refractory to chronic *in vivo* electrophysiology. We report a non-surgical method to achieve chronically stable *in vivo* recordings from single retinal ganglion cells (RGCs) in awake mice. We develop a non-coaxial intravitreal injection scheme in which injected mesh electronics unrolls inside the eye and conformally coats the highly curved retina without compromising normal eye functions. The method allows 16-channel recordings from multiple types of RGCs with stable responses to visual stimuli for at least two weeks, and reveals circadian rhythms in RGC responses over multiple day/night cycles

Main Text

As an approachable part of the brain, the retina provides an excellent model for analyzing the assembly and function of information-processing circuits in the central nervous system (CNS) (1, 2). Interneurons receive signals from light-sensitive photoreceptors (rods and cones) and pass it to retinal ganglion cells (RGCs), which send axons through the optic nerve to visual areas of the brain. Whereas photoreceptors are akin to pixels, information processing by interneurons renders each of ~40 types of RGCs selectively responsive to specific visual features such as motion or color contrasts (2–4). However, whereas *in vivo* single-neuron recordings in awake, behaving animals are routine for many parts of the brain (5, 6), analysis of RGCs has relied primarily on *ex vivo* electrophysiological recording (7, 8) and calcium imaging (4). Although these *ex vivo* studies have provided deep insights into retinal computations, they are limited in several respects. First, systemic effects, such as

*Corresponding author. cml@cmliris.harvard.edu.

†These authors contributed equally to this work.

neuromodulation, alterations in hormonal milieu and circadian variation, are difficult to study *ex vivo* (9–12). Second, recordings are limited to the short life-time of the preparation, typically a few hours, compromising the ability to detect plasticity in activity patterns. Third, rod function is prone to rapid loss in explants partly due to its dependence on pigment epithelium, which is generally removed during explantation. Therefore, *ex vivo* recordings of rod activities over extended times have remained challenging (4). Finally, it is obviously infeasible to correlate retinal activity *ex vivo* with organismic responses or behaviors. *In vivo* RGC electrophysiology could offer insight into the interaction between retina and related brain regions involved in vision processing and regulation (9, 13–15), yet existing technologies either have been unable to achieve single RGC resolution recordings in mice (11), or have been limited to 1–2 channels acute recording in anesthetized animals with larger eyes (16, 17).

We report chronically stable *in vivo* recordings from functionally-diverse RGCs in awake mice using epiretinal-implanted mesh electronics delivered via non-coaxial and minimally-invasive intravitreal injection to form a chronically-stable conformal retina interface. We designed a 16-channel mesh electronics probe with recording electrodes distributed evenly over a 1.5 mm × 0.8 mm region in 4 parallel rows to ensure coverage and interrogation of a large-area of the retina following injection. The 16 recording electrodes (green arrow, Fig. 1A, I) are individually addressable through polymer-encapsulated metal interconnect lines that terminate at input/output (I/O) pads (red arrow, Fig. 1A, I), which provide connection to external recording instrumentation. The tissue-like mesh electronics probes were fabricated using standard photolithography (18–22), with ~90% porosity in two-dimensions (2D) and mesh ribbon element widths = 10 μm to facilitate syringe injection through capillary needles and to minimize interference with the retina.

The three-dimensional (3D) highly curved concave mouse retina precludes using conventional methods, such as silicon, glass or metal electrodes (7, 16, 23) or planar microelectrodes arrays (8), to form a conformal and chronically stable retina interface. Therefore, we asked if the unique unrolling/unfolding capability of mesh electronics in aqueous solutions (19) could occur in the very low Young's modulus vitreous humor of the eye (24). This scheme could enable delivery of a large mesh (>1 mm²) through a much smaller non-surgical injection hole (<0.1 mm²). To deliver the mesh electronics into a mouse eye and form a conformal interface, a controlled non-coaxial injection scheme (Fig. 1A, II and III) was developed with several key features. First, the intravitreal injection procedure is compatible with standard stereotaxic frames commonly used for brain probe implantation (fig. S1, A and B). Second, the ultra-flexibility of mesh electronics enables loading and controlled injection into the eye through the lateral canthus using a small (330 μm outer diameter) glass capillary needle (blue arrows, fig. S1B and fig. S2, A and B) that is similar in diameter to 29-gauge needles commonly used for intraocular injection of virus vectors and drugs (25). Third, synchronizing the volumetric flow with the lateral motion of the needle to follow the curvature of the retina afforded lateral positioning and conformal coating of mesh electronics onto the concave retina surface (Fig. 1A, III, fig. S1C and fig. S3). After injection and needle withdrawal, the mesh was glued externally (fig. S2, C and D) (22) and the I/O pads were connected to an interface cable (flexible flat cable, or FFC), which was mounted on top of the skull, for electrical recording (20). The demonstrated

injection of mesh electronics into the mouse eye represents a challenging case; we expect that this method could be readily adapted for animals with larger and less curved eyes, including nonhuman primates.

To verify that mesh electronics, which is elastically-strained when loaded into the capillary needle (19), unrolls from the capillary to cover the retina after non-coaxial intravitreal injection, we devised a method for non-invasive in vivo through-lens imaging based on a liquid Hruby lens (Fig. 1B and fig. S4) (22). Both mesh electronics and retinal vasculature were visualized from Day 0 to 14 following injection. Quantitative analysis of the locations of representative recording electrodes demonstrated minimal variation of electrode positions over 14 days (table S1) (22). We also performed confocal microscopic imaging of the mesh-retina interface following dissection of mesh-injected eyes from TYW3 transgenic mice in which a subset of RGCs was labeled with yellow fluorescent protein (26) on Day 0 and 7 post-injection. Images (Fig. 1C, I) (22) showed that the mesh conformed to the concave structure of the retina with a mean distance of $51 \pm 35 \mu\text{m}$ (mean \pm SD) between an electrode and the closest labelled RGC. Given that only 10% of RGCs are labeled in the TYW3 mouse retina (27), the nearest RGC is likely closer than this mean distance. Higher-resolution images (Fig. 1C, II) further showed that the average soma diameter of RGCs, $12.2 \pm 1.9 \mu\text{m}$ (mean \pm SD), was similar to the $10 \mu\text{m}$ width of mesh elements and the density of labeled RGCs, $353 \text{ cells}/\text{mm}^2$, was within the reported range of $200\text{--}400 \text{ cells}/\text{mm}^2$ for YFP-labeled RGCs in the central retina of TYW3 mice (27). Together, the in vivo and ex vivo images confirmed a chronically stable, conformal and intimate interface between the 3D curved retina and the injected mesh electronics with no observable perturbation of RGC density or distribution.

Due to the rigidity of conventional probes used for single channel in vivo retina recording in larger animals, sutures and fixation rings are usually used to suppress the normal motor functions of the eye even when the animals are anesthetized (16, 28). We asked if we could take advantage of the ultraflexibility of mesh electronics to minimize interference with normal eye functions during recording in awake mice. First, we used near-infrared (NIR) imaging (13) to track eye responses during air puffs. Chronic studies of the blink reflex exhibited immediate and complete responses to timed air puffs (fig. S5A) with no statistically significant difference between mesh-implanted and control eyes (fig. S5C, I). Second, to assess retinal responsiveness to light, we measured the pupillary response as a function of ambient light intensity modulation for control eyes and mesh-injected eyes (fig. S5B and movie S1). We detected prompt and full-scale pupil expansion and shrinkage in response to increases and decreases in brightness, respectively (fig. S5C, II). Quantification of pupil constriction (22) revealed no statistically significant difference between control eyes and mesh-injected eyes (Fig. 1D, I). Third, to assess the influence of injected mesh on normal eye movement, we characterized the optokinetic reflex (OKR) in response to moving gratings (29). Consistent amplitude, temporal pattern, directionality and speed of OKR were observed between the control and injected eyes (fig. S5D). Quantitative analyses of the eye movement frequency showed no statistically significant difference between the mesh-injected and control eyes (Fig. 1D, II), both of which are also consistent with previous reports (30). Last, to evaluate the impact of injected mesh on visual acuity, we measured the OKR in response to moving gratings with varying spatial frequencies, and found the same

visual acuity of the mesh-injected eyes as the control (~ 0.4 cycles per degree; Fig. 1D, III) (31). It is also worth noting that the transparent polymer comprising the mesh scaffold with $< 5\%$ space occupied by metal features yields minimal blockage of incoming light as evidenced by the $\sim 95\%$ light transmittance in the 400–600 nm spectral window visible to the mouse (32) (fig. 5C, II, inset), resulting in negligible distortion of visual input. Taken together, these data demonstrate minimal damage of mesh injection to the orbicularis oculi, iris dilator and extraocular muscles as well as negligible interference with light perception and visual acuity of the retina.

Having demonstrated that mesh electronics has negligible effect on normal visual functions, we conducted a series of tests to probe their ability to detect the diverse RGC activities. First, we asked how many of the 16 channels in the implanted mesh electronics probe were sufficiently close to RGCs to record single-unit activity. Fig. 2A and fig. S6A show examples from two mice in which we obtained high quality recordings from all 16 channels, with a signal-to-noise ratio (SNR) > 7 for single-unit spikes. Moreover, single-unit activity was detected in at least 12 channels from each of 5 separate mice, thus highlighting the robustness of the injected mesh electronics probes for multiplexed retinal electrophysiology.

Second, we asked whether we could record repeatedly from the same sets of RGCs. Multiplexed 16-channel recordings revealed that the SNR from all channels remains > 7 for single-unit spikes on Days 3 and 14 with little variation in SNR for each specific channel (Fig. 2A,B and fig. S7A). The ON/OFF light response in these two representative channels (Ch2 and Ch8, Fig. 2C,D), which included four RGC neurons (two for each channel) identified by spike sorting, also demonstrated statistically significant differences in modulation of firing patterns (Fig. 2E). Specifically, analysis of the variance (ANOVA) showed a statistically significant (P value < 0.01) difference in firing rate between ‘ON’ and ‘OFF’ phases of light modulation, but no significant (P value > 0.05) difference during the same ‘ON’ or ‘OFF’ phase at different days (22). Furthermore, analyses of the ON-OFF indices (4, 22) yielded values of 0.97 and 0.91 for the two Ch2 neurons and -0.74 and -0.55 for the two Ch8 neurons, showing that the two Ch2 and two Ch8 neurons can be identified as ON and OFF RGCs, respectively.

Third, we asked whether it was possible to assess the chronic stability and behavior of individual RGCs. We implemented a spike sorting protocol to identify and cluster single-units based on principal component analysis (PCA) (22, 33). L-ratio analysis (table S2) (34) together with characterization of the number and spike waveforms of detected neurons from all 16 channels on Day 3 and 14 (fig. S7B) indicate good unit separation and chronic recording stability. Furthermore, systematic characterization from the two representative channels (Ch2 and Ch8, Fig. 2, C and D, right column) from day 0 through 14 shows similar average spike waveforms indicative of chronic recording stability (fig. S8A). Moreover, quantitative waveform autocorrelation analyses (fig. S8B) (35) show that the same four neurons were stably tracked across this period. Altogether, we isolated 134 single units from 89 channels from 5 mice with chronic stability; additional examples are described below.

Fourth, to assess the range of RGC types we could detect, we stimulated the retinas in awake mice with a spatially-varying grating designed to elicit responses from direction-selective

(DS) and orientation-selective (OS) RGCs and investigated the capability to engage the same DS and OS RGCs chronically (22). The multiplexed measurements were made with the head rigidly restrained (white arrow, Fig. 3, A and B) to ensure a fixed visual field with respect to the moving grating displayed on a flat screen (movie S2) with alternating 2-second ON and OFF periods (pink and white vertical bars, Fig. 3C). Representative raster plot data from one of these channels on Day 7 and Day 14 (Fig. 3C and fig. S6, B and C) highlight the chronically-stable behavior, including spike waveforms, amplitudes and raster plot responses, of three spike-sorted RGCs. Specifically, average spike waveforms for these three neurons in the 10 trials each day and between Day 7 and 14 exhibit minimal systematic change (fig. S9A), which was confirmed by auto-and cross-correlation analyses (fig. S9B). Moreover, polar plots of firing rate versus grating direction (right, Fig. 3C) show that these three neurons can be classified as follows: neuron-1 (red) is a direction selective ganglion cell (DSGC) with nasal-to-temporal (N→T) preference, neuron-2 (green) is a non-DSGC, and neuron-3 (blue) is a DSGC with ventral-to-dorsal (V→D) preference. The direction preference and selectivity from Day 7 to 14 post-injection were stable and small variations between days were statistically insignificant (fig. S9, C & D). We note that the intact OKR driven by the moving gratings did not disrupt the chronic RGC recording stability (fig. S10), and that potential OKR-induced random variability was averaged from RGC responses over 10 consecutive trials of moving grating stimulation (36).

A summary of our in vivo 16-channel measurements from Day 7 to 14 (Fig. 3D; fig. S11) confirm the stable chronic recording across all channels. Overall, we recorded from 32 RGCs of which 15 were non-DSGCs, 3 were orientation selective (OSGCs; 2 dorsal-ventral & 1 nasal-temporal) and 14 were direction selective (2 D→V, 5 V→D, 3 N→T & 4 T→N) (22). The direction selectivity indices (DSi's) (22) remained stable and no RGCs shifted categories between the two recording sessions (days 7 and 14), providing additional evidence that individual cells can be tracked for 2 weeks (Fig. 3E). Moreover, the percentages of DSGCs, OSGCs and non-DSGCs (44%, 9% and 47%, respectively) in this data set are similar to those obtained from recent large-scale calcium imaging of >5,000 RGCs in retinal explants (35%, 14.5% and 51.5%; difference between the two data sets P value > 0.05 by chi square test)(4).

Finally, we asked whether we could use implanted mesh electronics to investigate circadian modulation of RGC activity (22). Specifically, we monitored RGCs at 4 hour intervals over several day/night cycles (Fig. 4A) for a total of 18 recordings (nocturnal, 8pm – 8am; diurnal, 8am – 8pm). Representative data from a DSGC in a mouse demonstrated that preferred direction and direction selectivity varied little during this period (fig. S12A). In contrast, the absolute firing rate in the preferred direction ($\pm 45^\circ$) varied in a consistent way over three complete circadian cycles (Days 1–2, 4–5 and 6–7 after injection), with on average a 77% higher firing rate during the diurnal phase than the nocturnal phase (Fig. 4B). Similar constancy of preferred direction but circadian variation of activity level was found for other RGCs, including a D→VDSGC and a non-DSGC (fig. S12, B and C).

Overall, of the 28 RGCs from 3 mice we recorded in this regime, 20 exhibited higher firing rates during the diurnal phase. Four others exhibited decreased firing rates during the diurnal phase and the remaining four showed minimal circadian modulation, based on their

circadian modulation indices (CMi's; Fig. 4, C and D) (22). Cells that were tracked for three complete circadian cycles demonstrated that RGCs remained in the same circadian modulation categories despite slight variations in CMi values (Fig. 4E). Interestingly, of 6 cells for which ON-OFF preferences were measured carefully, 2/3 diurnal-high cells were ON and one was ON-OFF, 2/2 nocturnal-high cells were OFF and the sole invariant cell was ON-OFF, suggesting a correlation between RGC polarity and day/night modulation of activity that will be interesting to investigate in the future. The pattern of increased diurnal firing activity for the majority of RGCs is consistent with results of a previous ERG study in which the b-wave amplitude, which reflects population average of ON-bipolar cell activity (37), was found to increase in the daytime(11).

In summary, we have demonstrated multiplexed, chronically stable recording from diverse RGC types using syringe-injectable mesh electronics in mice. The ultra-flexibility of mesh electronics allowed for non-surgical intravitreal delivery into mouse eyes via non-coaxial injection and formation of conformal and chronically stable functional interface with the retina in vivo, which can be readily adapted for other animals with bigger eyes. This method provides an attractive alternative to past studies of RGC activity in explants and offers important new insights into the dynamic information processing between the retina and other parts of the CNS that is impossible to obtain from retinal explants.

Supplementary Material

Refer to Web version on PubMed Central for supplementary material.

Acknowledgments

We thank Prof. J. E. Dowling for helpful discussions, Prof. M. Meister for useful suggestions and Dr. J. Huang for help with recording instrumentation. C.M.L. acknowledges support of this work by the Air Force Office of Scientific Research, Harvard University Physical Sciences and Engineering Accelerator award, and a National Institutes of Health Director's Pioneer Award (1DP1EB025835-01). G.H. acknowledges support of this work by the American Heart Association Postdoctoral Fellowship (16POST27250219) and the Pathway to Independence Award (Parent K99/R00) from the National Institute on Aging of the National Institutes of Health (1K99AG056636-01). M.Q. and J.R.S. were supported by R37 NS029169 from NINDS. This work was performed in part at the Harvard University Center for Nanoscale Systems (CNS), a member of the National Nanotechnology Coordinated Infrastructure Network (NNCI), which is supported by the National Science Foundation.

References and Notes

1. Masland RH. The neuronal organization of the retina. *Neuron*. 2012; 76:266–280. [PubMed: 23083731]
2. Hoon M, Okawa H, Della Santina L, Wong RO. Functional architecture of the retina: development and disease. *Prog Retin Eye Res*. 2014; 42:44–84. [PubMed: 24984227]
3. Sanes JR, Masland RH. The Types of Retinal Ganglion Cells: Current Status and Implications for Neuronal Classification. *Annu Rev Neurosci*. 2015; 38:221–246. [PubMed: 25897874]
4. Baden T, et al. The functional diversity of retinal ganglion cells in the mouse. *Nature*. 2016; 529:345–350. [PubMed: 26735013]
5. Lewis CM, Bosman CA, Fries P. Recording of brain activity across spatial scales. *Curr Opin Neurobiol*. 2015; 32:68–77. [PubMed: 25544724]
6. Hamel EJ, Grewe BF, Parker JG, Schnitzer MJ. Cellular level brain imaging in behaving mammals: an engineering approach. *Neuron*. 2015; 86:140–159. [PubMed: 25856491]

7. Kim IJ, Zhang YF, Yamagata M, Meister M, Sanes JR. Molecular identification of a retinal cell type that responds to upward motion. *Nature*. 2008; 452:478–482. [PubMed: 18368118]
8. Field GD, et al. Functional connectivity in the retina at the resolution of photoreceptors. *Nature*. 2010; 467:673–U654. [PubMed: 20930838]
9. LeGates TA, Fernandez DC, Hattar S. Light as a central modulator of circadian rhythms, sleep and affect. *Nat Rev Neurosci*. 2014; 15:443–454. [PubMed: 24917305]
10. Korshunov KS, Blakemore LJ, Trombley PQ. Dopamine: A Modulator of Circadian Rhythms in the Central Nervous System. *Front Cell Neurosci*. 2017; 11:91. [PubMed: 28420965]
11. Jackson CR, et al. Retinal dopamine mediates multiple dimensions of light-adapted vision. *J Neurosci*. 2012; 32:9359–9368. [PubMed: 22764243]
12. Hwang CK, et al. Circadian Rhythm of Contrast Sensitivity Is Regulated by a Dopamine-Neuronal PAS-Domain Protein 2-Adenylyl Cyclase 1 Signaling Pathway in Retinal Ganglion Cells. *J Neurosci*. 2013; 33:14989–14997. [PubMed: 24048828]
13. Liu BH, Huberman AD, Scanziani M. Cortico-fugal output from visual cortex promotes plasticity of innate motor behaviour. *Nature*. 2016; 538:383–387. [PubMed: 27732573]
14. Wilson DE, Whitney DE, Scholl B, Fitzpatrick D. Orientation selectivity and the functional clustering of synaptic inputs in primary visual cortex. *Nat Neurosci*. 2016; 19:1003–1009. [PubMed: 27294510]
15. Dhande OS, Huberman AD. Retinal ganglion cell maps in the brain: implications for visual processing. *Curr Opin Neurobiol*. 2014; 24:133–142. [PubMed: 24492089]
16. Kuffler SW. Discharge patterns and functional organization of mammalian retina. *J Neurophysiol*. 1953; 16:37–68. [PubMed: 13035466]
17. Barlow HB, Hill RM, Levick WR. Retinal Ganglion Cells Responding Selectively to Direction and Speed of Image Motion in the Rabbit. *J Physiol*. 1964; 173:377–407. [PubMed: 14220259]
18. Fu TM, et al. Stable long-term chronic brain mapping at the single-neuron level. *Nat Methods*. 2016; 13:875–882. [PubMed: 27571550]
19. Liu J, et al. Syringe-injectable electronics. *Nat Nanotechnol*. 2015; 10:629–636. [PubMed: 26053995]
20. Hong GS, et al. Syringe Injectable Electronics: Precise Targeted Delivery with Quantitative Input/Output Connectivity. *Nano Lett*. 2015; 15:6979–6984. [PubMed: 26317328]
21. Zhou T, et al. Syringe-injectable mesh electronics integrate seamlessly with minimal chronic immune response in the brain. *Proc Natl Acad Sci USA*. 2017; 114:5894–5899. [PubMed: 28533392]
22. Materials and methods are available as supplementary materials at the *Science* website.
23. Jun JJ, et al. Fully integrated silicon probes for high-density recording of neural activity. *Nature*. 2017; 551:232–236. [PubMed: 29120427]
24. Nickerson CS, Karageozian HL, Park J, Kornfield JA. The mechanical properties of the vitreous humor. *Invest Ophth Vis Sci*. 2004; 45:37.
25. Duan X, et al. Subtype-Specific Regeneration of Retinal Ganglion Cells following Axotomy: Effects of Osteopontin and mTOR Signaling. *Neuron*. 2015; 85:1244–1256. [PubMed: 25754821]
26. Kim IJ, Zhang YF, Meister M, Sanes JR. Laminar Restriction of Retinal Ganglion Cell Dendrites and Axons: Subtype-Specific Developmental Patterns Revealed with Transgenic Markers. *J Neurosci*. 2010; 30:1452–1462. [PubMed: 20107072]
27. Zhang YF, Kim IJ, Sanes JR, Meister M. The most numerous ganglion cell type of the mouse retina is a selective feature detector. *Proc Natl Acad Sci USA*. 2012; 109:E2391–E2398. [PubMed: 22891316]
28. Suematsu N, Naito T, Miyoshi T, Sawai H, Sato H. Spatiotemporal receptive field structures in retinogeniculate connections of cat. *Front Syst Neurosci*. 2013; 7:103. [PubMed: 24367299]
29. Zoccolan D, Graham BJ, Cox DD. A self-calibrating, camera-based eye tracker for the recording of rodent eye movements. *Front Neurosci*. 2010; 4:193. [PubMed: 21152259]
30. Yonehara K, et al. Congenital Nystagmus Gene FRMD7 Is Necessary for Establishing a Neuronal Circuit Asymmetry for Direction Selectivity. *Neuron*. 2016; 89:177–193. [PubMed: 26711119]

31. Prusky GT, Alam NM, Beekman S, Douglas RM. Rapid quantification of adult and developing mouse spatial vision using a virtual optomotor system. *Invest Ophthalmol Vis Sci.* 2004; 45:4611–4616.
32. Jacobs GH, Williams GA, Cahill H, Nathans J. Emergence of novel color vision in mice engineered to express a human cone photopigment. *Science.* 2007; 315:1723–1725. [PubMed: 17379811]
33. Quiroga RQ, Nadasdy Z, Ben-Shaul Y. Unsupervised spike detection and sorting with wavelets and superparamagnetic clustering. *Neural Comput.* 2004; 16:1661–1687. [PubMed: 15228749]
34. Schmitzer-Torbert N, Redish AD. Neuronal activity in the rodent dorsal striatum in sequential navigation: separation of spatial and reward responses on the multiple T task. *J Neurophysiol.* 2004; 91:2259–2272. [PubMed: 14736863]
35. Jackson A, Fetz EE. Compact movable microwire array for long-term chronic unit recording in cerebral cortex of primates. *J Neurophysiol.* 2007; 98:3109–3118. [PubMed: 17855584]
36. Sun W, Tan Z, Mensh BD, Ji N. Thalamus provides layer 4 of primary visual cortex with orientation- and direction-tuned inputs. *Nat Neurosci.* 2016; 19:308–315. [PubMed: 26691829]
37. Gurevich L, Slaughter MM. Comparison of the waveforms of the ON bipolar neuron and the b-wave of the electroretinogram. *Vision Res.* 1993; 33:2431–2435. [PubMed: 8249322]
38. Fu TM, Hong G, Viveros RD, Zhou T, Lieber CM. Highly scalable multichannel mesh electronics for stable chronic brain electrophysiology. *Proc Natl Acad Sci USA.* 2017; 114:E10046–E10055. [PubMed: 29109247]
39. Xie Z, et al. Safety and efficacy of intravitreal injection of recombinant erythropoietin for protection of photoreceptor cells in a rat model of retinal detachment. *Eye.* 2012; 26:144–152. [PubMed: 22020175]
40. Hruby K. Slit Lamp Microscopy of the Posterior Section of the Eye with the New Preset Lens. *Arch Ophthalmol.* 1950; 43:330–336.
41. Thompson S, et al. Different inner retinal pathways mediate rod-cone input in irradiance detection for the pupillary light reflex and regulation of behavioral state in mice. *Invest Ophthalmol Vis Sci.* 2011; 52:618–623. [PubMed: 20847113]
42. Jones IL, et al. A method for electrophysiological characterization of hamster retinal ganglion cells using a high-density CMOS microelectrode array. *Front Neurosci.* 2015; 9:360. [PubMed: 26528115]
43. Schmitzer-Torbert N, Jackson J, Henze D, Harris K, Redish AD. Quantitative measures of cluster quality for use in extracellular recordings. *Neuroscience.* 2005; 131:1–11. [PubMed: 15680687]
44. Kondo S, Ohki K. Laminar differences in the orientation selectivity of geniculate afferents in mouse primary visual cortex. *Nat Neurosci.* 2016; 19:316–319. [PubMed: 26691830]

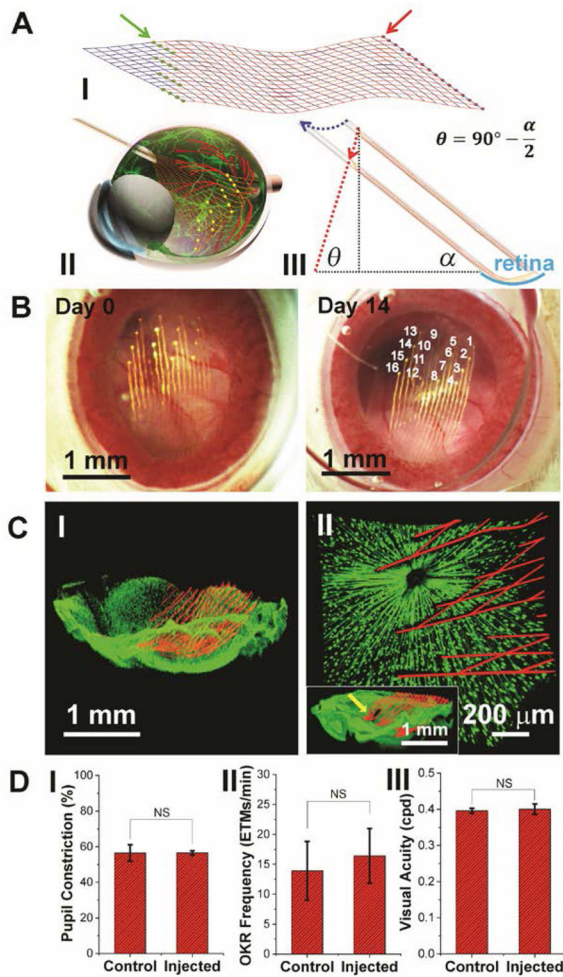


Fig. 1. Non-coaxial intravitreal injection and conformal coating of mesh electronics on the mouse retina

(A) **I**, Schematic showing the layout of mesh electronics comprising 16 recording electrodes (green dots indicated by a green arrow) and I/O pads (red dots indicated by a red arrow). **II**, Schematic showing non-coaxial intravitreal injection of mesh electronics onto the RGC layer. Multiplexed recording electrodes are shown as yellow dots. **III**, Schematic of non-coaxial injection that allows controlled positioning of mesh electronics on the concave retina surface (cyan arc). The blue and red dotted arrows indicate the motion of the needle and desired trajectory of the top end of the mesh, respectively (see fig. S1 for details) (22). (B) In vivo through-lens images of the same mouse eye fundus on Day 0 and Day 14 post-injection of mesh electronics, with electrode indexing in the Day 14 image (22). (C) Ex vivo imaging of the interface between injected mesh electronics (red, mesh polymer elements) and the retina (green dots, RGCs) on Day 0 (**I**) and 7 (**II**) post-injection. The inset of **II** shows the region indicated by a yellow arrow where the high-resolution image was taken (22). (D) Comparison of pupillary reflex ($n = 3$), OKR ($n = 5$) and visual acuity ($n = 3$) between control and injected mouse eyes. The error bars indicate ± 1 standard deviation (s.d.). NS, not significant ($P > 0.05$). One-way ANOVA test is used for statistical analyses.

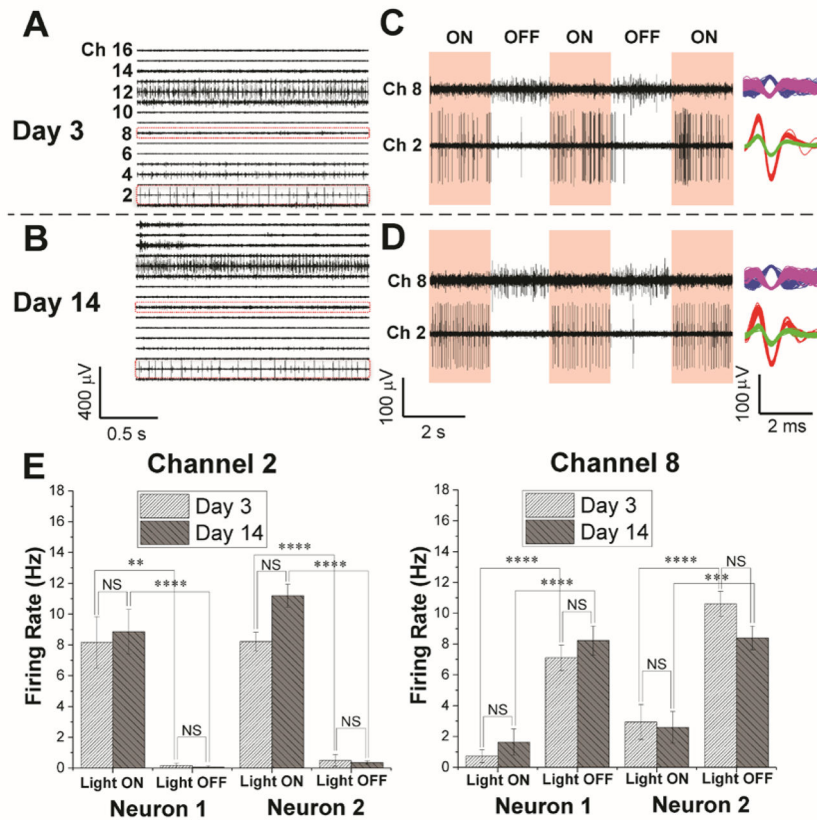


Fig. 2. Chronic 16-channel in vivo electrophysiology of single RGCs measured with mesh electronics

(**A** and **B**) Representative 16-channel recordings from the same mesh electronics delivered onto a mouse retina on Day 3 (**A**) and 14 (**B**) post-injection. (**C** and **D**) Light modulation of two representative channels (Ch2 and Ch8) in red dashed boxes in panels (**A**) and (**B**) on Day 3 (**C**) and 14 (**D**) post-injection. The red shaded and unshaded regions indicate the light 'ON' and 'OFF' phases, respectively. Representative sorted spikes assigned to different neurons on both days are shown in the rightmost column for each channel. Each distinct color in the sorted spikes represents a unique identified neuron. (**E**) Firing rates of all sorted neurons from Ch2 and Ch8 during light modulations on Day 3 and 14 post-injection (22). The error bars indicate ± 1 standard error of the mean (s.e.m.). **, ***, **** indicate P value of < 0.01 , < 0.001 , < 0.0001 , respectively, and NS is not significant ($P > 0.05$), respectively. One-way ANOVA test is used for statistical analyses. $n = 5$ for mice used for multiplexed recordings.

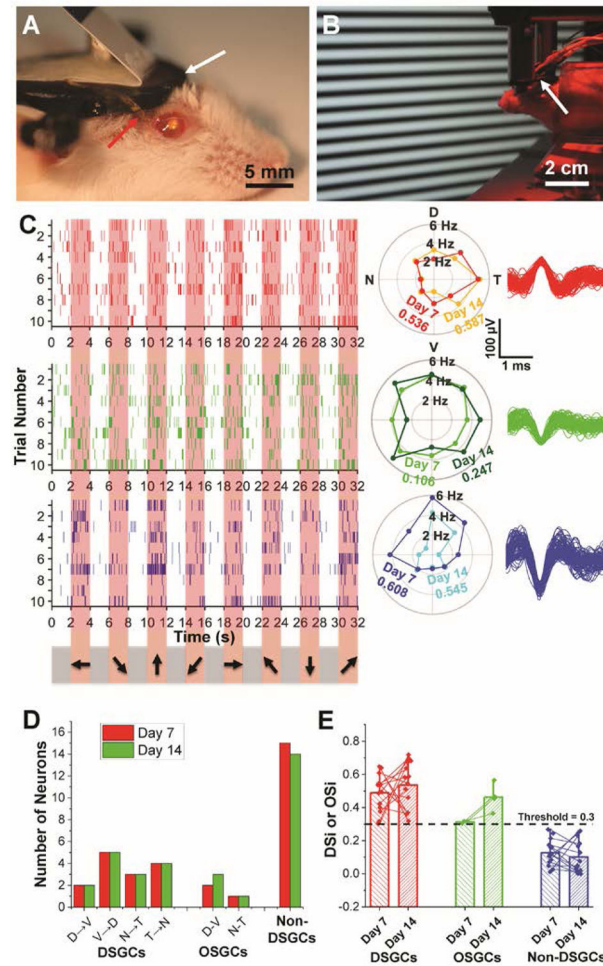


Fig. 3. Chronic in vivo recording and tracking of the same DSGCs

(A) Photograph showing a mouse immediately after mesh injection. The red and white arrows indicate part of mesh electronics outside of the eye and a head-plate for head fixation. (B) Red-light photograph showing in vivo recording of DSGCs in response to moving grating stimulations (22). (C) Raster (left), polar plots (center) and overlaid spike waveforms (right) of single-unit firing events of three neurons with corresponding colors, from Ch8 in response to moving grating stimulations on Day 7 and 14 post-injection. In the raster plots, the pink shaded regions correspond to times when gratings were displayed on the screen with moving directions indicated by arrows on the bottom (22). Only the raster plots on Day 7 are shown. In the polar plots, DSi for each cell on different days is labeled with corresponding colors. (D) Bar chart summarizing numbers of identified DSGCs, OSGCs and non-DSGCs on Day 7 (red bars) and Day 14 (green bars) post-injection. (E) Bar chart with overlaid scatter plot of DSi or OSi of all RGCs on Day 7 and 14, with thin lines of corresponding colors connecting the same neurons identified on both days. The bar height and the whisker indicate the mean and maximum of DSi/OSi values, respectively. $n = 4$ for mice used for direction and orientation selectivity studies, while data from one representative mouse is shown in this figure.

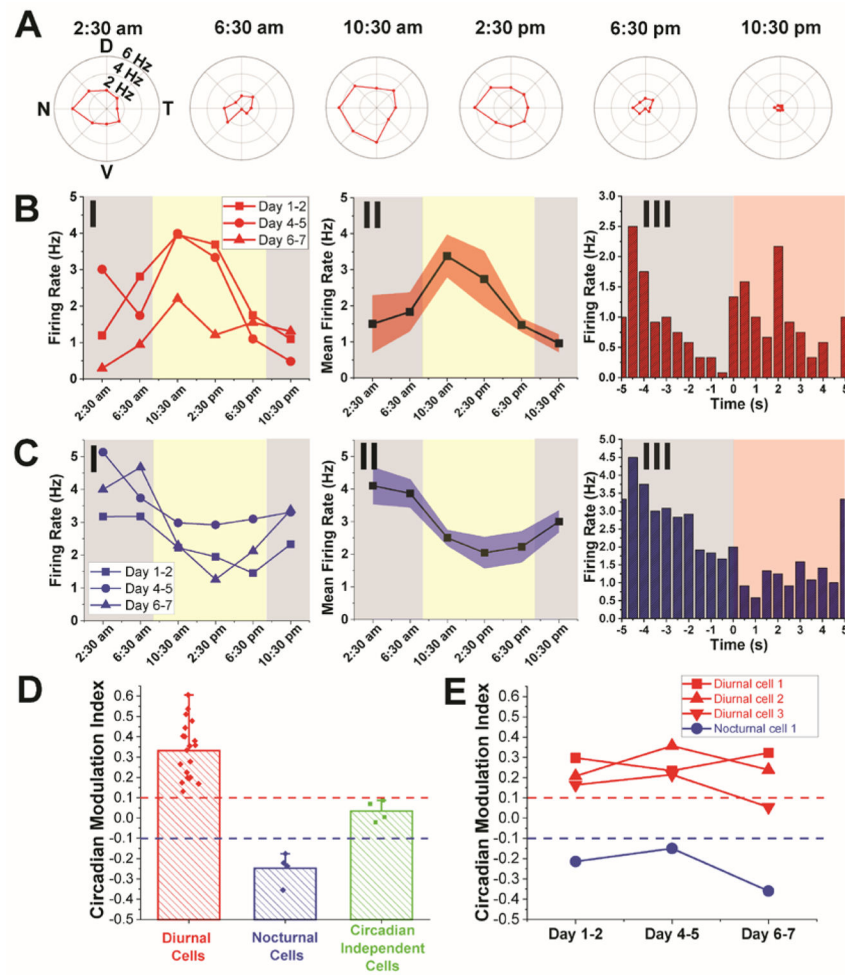


Fig. 4. Chronic circadian modulation of individual RGC activity
(A) Representative polar plots of a DSGC at different times in one complete circadian cycle on Days 4–5 post-injection. All graphs are plotted in same range of firing frequencies. **(B)** Firing rates of the same DSGC in **(A)** averaged over preferred directions in three complete circadian cycles on Days 1–2, 4–5 and 6–7 post-injection **(I)**, and the mean firing rate by taking the average over these three circadian cycles **(II)**. This DSGC is identified as an ON-OFF transient type **(III)**. **(C)** Firing rates of another DSGC averaged over preferred directions on three complete circadian cycles on Days 1–2, 4–5 and 6–7 post-injection **(I)**, and the mean firing rate by taking the average over these three circadian cycles **(II)**. This DSGC is identified as an OFF transient type **(III)**. The yellow and gray shaded regions in panels **I** and **II** of both **(B)** and **(C)** indicate diurnal and nocturnal circadian times, respectively, while the red shaded and white regions in panel **III** of both **(B)** and **(C)** indicate light ON and OFF phases, respectively. Red and blue shaded regions in panels **(B)**, **II** and **(C)**, **II** reflect ± 1 s.e.m. **(D)** Bar chart with overlaid scatter plot of the CMi of diurnal cells (red bars), nocturnal cells (blue bars) and circadian independent cells (green bars) (22). The bar height and the whisker indicate the mean and maximum of CMi values, respectively. **(E)** Plots showing the evolution of CMi values for four representative cells (three diurnal cells and one nocturnal cells) that were recorded for three complete circadian cycles. Red and

blue dashed lines in both **(D)** and **(E)** indicate the threshold for defining diurnal and nocturnal cells, respectively. $n = 3$ for mice used for circadian modulation study of RGC activity.

Author Manuscript

Author Manuscript

Author Manuscript

Author Manuscript